nanomaterials

MDPI

Article

Efficient $ReSe_2$ Photodetectors with CVD Single-Crystal Graphene Contacts

Bruna Silva [1,2], João Rodrigues [1], Balaji Sompalle [1,2], Chun-Da Liao [1], Nicoleta Nicoara [1], Jérôme Borme [1], Fátima Cerqueira [1,2], Marcel Claro [1], Sascha Sadewasser [1], Pedro Alpuim [1,2] and Andrea Capasso [1,*]

[1] International Iberian Nanotechnology Laboratory, 4715-330 Braga, Portugal; bruna.silva@inl.int (B.S.); joao.rodrigues@inl.int (J.R.); sgds.balaji@gmail.com (B.S.); chundaliao@ntu.edu.tw (C.-D.L.); nicoleta.nicoara@inl.int (N.N.); jerome.borme@inl.int (J.B.); fatima.cerqueira@inl.int (F.C.); marcel.claro@inl.int (M.C.); sascha.sadewasser@inl.int (S.S.); pedro.alpuim.us@inl.int (P.A.)

[2] Centre of Physics, University of Minho, 4710-057 Braga, Portugal

* Correspondence: andrea.capasso@inl.int

Abstract: Rhenium-based 2D transition metal dichalcogenides such as $ReSe_2$ are suitable candidates as photoactive materials for optoelectronic devices. Here, photodetectors based on mechanically exfoliated $ReSe_2$ crystals were fabricated using chemical vapor deposited (CVD) graphene single-crystal (GSC) as lateral contacts. A "pick & place" method was adopted to transfer the desired crystals to the intended position, easing the device fabrication while reducing potential contaminations. A similar device with Au was fabricated to compare contacts' performance. Lastly, a CVD hexagonal boron nitride (hBN) substrate passivation layer was designed and introduced in the device architecture. Raman spectroscopy was carried out to evaluate the device materials' structural and electronic properties. Kelvin probe force measurements were done to calculate the materials' work function, measuring a minimal Schottky barrier height for the GSC/$ReSe_2$ contact (0.06 eV). Regarding the electrical performance, I-V curves showed sizable currents in the GSC/$ReSe_2$ devices in the dark and under illumination. The devices presented high photocurrent and responsivity, along with an external quantum efficiency greatly exceeding 100%, confirming the non-blocking nature of the GSC contacts at high bias voltage (above 2 V). When introducing the hBN passivation layer, the device under white light reached a photo-to-dark current ratio up to 10^6.

Keywords: 2D materials; transition metal dichalcogenides; van der Waals heterostructures; hexagonal boron nitride; CVD; optoelectronics; contact barrier height

Citation: Silva, B.; Rodrigues, J.; Sompalle, B.; Liao, C.-D.; Nicoara, N.; Borme, J.; Cerqueira, F.; Claro, M.; Sadewasser, S.; Alpuim, P.; et al. Efficient $ReSe_2$ Photodetectors with CVD Single-Crystal Graphene Contacts. *Nanomaterials* **2021**, *11*, 1650. https://doi.org/10.3390/nano11071650

Academic Editor: Gwan-Hyoung Lee

Received: 18 May 2021
Accepted: 18 June 2021
Published: 23 June 2021

1. Introduction

Transition metal dichalcogenides (TMDCs) are semiconductors of the MX_2 type, where M is a transition metal (e.g., molybdenum, rhenium, tungsten) and X is a chalcogen element (e.g., sulfur, selenium, and tellurium). This class of layered materials can be produced in two-dimensional (2D) form or thinned down to atomic thickness, i.e., by exfoliating the corresponding bulk crystals that have weak interlayer van der Waals bonding [1,2]. Two-dimensional TMDCs are structurally stable materials that exhibit interesting electronic and optical properties: direct and tunable bandgap, considerable exciton binding energy, high carrier mobility, strong spin-orbit coupling, strong photoluminescence (especially in monolayer form), and nonlinear optical properties [1,2]. As such, 2D TMDCs find potential applications in electronics, optoelectronics, photonics, sensing, and energy storage [3–7]. A key characteristic of atomically thin TMDCs is the possibility to select or grow crystals with a specific number of layers, thus tuning the optoelectronic properties to comply with device requirements [3]. However, this can translate into technical difficulties related to thickness control and sample uniformity. Recent studies on 2D rhenium-based dichalcogenide materials–ReX_2 (X = S or Se)–have shown optoelectronic properties that are independent of

the number of layers: Even in bulk, the layers act as electronically and vibrationally decoupled monolayers [8,9]. These features give ReX_2 an excellent potential for optoelectronic nano-devices and 2D heterostructures, releasing device fabrication and uniformity control constraints. For these reasons, and owing to their structural and electronic properties [9–14], ReX_2 has attracted significant scientific and technological interest [10,12,13,15]. In particular, $ReSe_2$ has a bandgap of ~1.3 eV [9] and is suitable for optoelectronic applications, although only a few groups tested it in transistors and photodetectors [15–19].

In the last years, several 2D TDMCs configurations (e.g., so-called van der Waals heterostructures) were proposed to improve the performance or unlock new functionalities in optoelectronics and spintronics [1,3–6]. Numerous approaches were proposed to make 2D heterostructures: mechanical exfoliation and sequential layer restacking, layer-by-layer chemical vapor deposition (CVD), or any combination of these approaches, each presenting its pros and cons. Mechanical exfoliation is a simple technique that can be coupled with the stamping method with the aid of polymeric viscoelastic stamps (e.g., PDMS) [20]. The device fabrication is quite versatile, but the throughput is extremely low. By contrast, CVD is suited for each layer's direct growth but requires rigorous control and optimization of the growth parameters and cannot grant control on the layer positioning and geometry: post-processing is thus required, which adds complexity to the whole device fabrication process. When making 2D TMDC-based electronic devices, it became apparent that input/output metallic contacts may introduce severe technical challenges [21–24]. A non-ohmic contact at a mismatched metal-semiconductor interface forms a Schottky barrier that can impact the device's functionality and performance. Consequently, the choice of optimal electrical contacts is crucial [24,25], as is the realization of ultra-clean interfaces among 2D TDMCs [26]. The properties of 2DMs are dependent on the surface chemistry and interface coupling to a large extent, so clean interfaces between different 2DMs are vital to maximizing the device performance [27]. As a contact material, graphene has a high thermal conductivity and electron mobility, but in polycrystalline graphene (i.e., the most common form) the transport largely depends on the grain boundary concentration [28]. The realization of graphene contacts is usually a versatile and non-damaging process that provides defect-free interfaces [29]. Graphene is often coupled with hexagonal boron nitride (hBN) layers, serving as a substrate or encapsulating layers, maximizing graphene's electronic performance. hBN is a large bandgap insulator (5.97 eV) [30], chemically inert, and free of dangling bonds or surface charge traps. It has a low lattice mismatch with graphene (1.7%) [31] providing effective passivation (e.g., on top of Si/SO_2 or as an interlayer in 2D van der Waals heterostructures) [32].

In this work, we fabricate photodetectors based on mechanically exfoliated $ReSe_2$ crystals. A "pick & place" method is adopted to (i) allow the identification of the most fitting $ReSe_2$ crystals among the wide range of exfoliated sizes and (ii) transfer the selected crystals to the desired location. Since this is an all-dry procedure, the possibility of additional contaminations is reduced. Using this technique, the semiconductor is interfaced with CVD GSC contacts in a lateral-heterostructure design. $ReSe_2$ serves as an efficient photoactive layer, while graphene can collect the charge carriers without introducing a sizeable Schottky junction at the interface [33]. A similar device with $Au/ReSe_2$ is fabricated to compare Gr and Au contacts' performance. Building on this design, a CVD hBN passivation layer is introduced to fabricate an $hBN/GSC/ReSe_2$ device with higher photoactive layer thickness. Raman spectroscopy of the device materials is carried out to evaluate the materials' structural and electronic properties. Kelvin probe force measurements (KPFM) are conducted to analyze and compare the $GSC/ReSe_2$ and $Au/ReSe_2$ devices' topography and work functions. To evaluate the electrical performance of the devices, I-V curves were acquired in the dark and illumination. The $Au/ReSe_2$ and $GSC/ReSe_2$ devices are tested under an intense white light to measure the photoconductivity as a function of the incident optical power by filtering the light beam with different neutral density filters, and also under 530 and 790 nm illumination, to calculate the external quantum efficiency (EQE). To study the $hBN/GSC/ReSe_2$ device photoconductivity, time-resolved photoresponse

is measured with a white light illumination and decay measurements are performed at increasing bias voltage.

2. Materials and Methods

2.1. CVD Growth and Transfer of Graphene and hBN

Graphene single crystals were grown on Cu foils via low-pressure CVD. A Cu foil substrate (25-µm-thick, Alfa Aesar, purity 99.8%), serving as a metal catalyst, was cleaned by an ultrasonic bath in a mixture of 20 mL 0.5 M $FeCl_3$, 20 mL 37% HCl and 360 mL de-ionized (DI) water, followed by rinsing in DI water. The Cu substrate was pre-oxidized by placing the foil onto a hotplate at 200 °C for 30 min. The Cu substrate is then loaded in a height-controlled sapphire cavity, placed in a 10 cm × 10 cm graphite box and loaded in the CVD tube. The substrate was annealed at 1040 °C for 30 min in Ar atmosphere (500 sccm, 9 Torr). For graphene growth, the gas mixture is switched to $Ar/H_2/CH_4$ (250/100/1.2 sccm, 4 Torr) keeping the temperature of 1040 °C for 40 min (temperature oscillations <0.5 °C). After the growth, the tube is cooled down to room temperature in Ar (500 sccm). hBN films were grown on Cu foil substrates in a CVD system with an independent pre-heating reservoir cell and an injector to deliver the precursor vapor over the substrate. 300 mg of ammonia borane (AB, H_3BNH_3, Sigma-Aldrich, St. Louis, MO, USA) were loaded in the reservoir cell and pre-heated at 80 °C (at 3 °C/min) for 4 h in H_2 atmosphere, and then let cool down to room temperature (at 3 °C/min). The pre-heating step serves to decompose AB into diammoniate of diborane ($[H_2B(NH_3)_2][BH_4]$, DADB), suppressing the melting point and allowing for a shorter deposition time under more stable growth conditions. The precursor vapor mixed to H_2 was allowed in the CVD tube where an Ar/H_2 mixture (200/50 sccm, at 2 Torr) carried it to the Cu substrate. For the growth of the hBN film, the temperature was set at 1000 °C for 15 min. After cooling down and extraction, the films were transferred onto Si/SiO_2 wafers by PMMA-assisted wet transfer [34].

2.2. Devices Fabrication

The fabrication of the GSC/$ReSe_2$ lateral-heterostructure device was carried out as follows. CVD-grown GSCs were transferred to a Si/SiO_2 substrate with TiWN crosshair markers by a similar PMMA-assisted wet transfer method as stated in ref. [34]: PMMA was spin-coated on Cu/GSCs as a sacrificial layer, and $FeCl_3$ (0.5M) was used as Cu etchant. After a 2 h etch, the PMMA/GSCs stack was cleaned in deionized water (DIW) three times before transferring to the final substrate, drying, and finally removing the PMMA (in acetone bath overnight at room temperature). Couples of neighboring GSCs suitable for the device fabrication were identified at the microscope and localized using the markers. An n-type $ReSe_2$ crystal (produced by M. Pumera's group [35]) was then placed across two neighboring GSCs to form a channel, using the "pick & place" method, described as follows. After mechanical exfoliation with Nitto tape (SPV 224), the $ReSe_2$ crystal was transferred to a viscoelastic PDMS (PF Gel-film from GelPak, Hayward, CA, USA). The crystal thickness and homogeneity were assessed at the microscope by evaluating the optical contrast. After identifying the desired crystal, it was transferred across the two GSCs on the Si/SiO_2 substrate. The PDMS + $ReSe_2$ stack was then mounted on a glass slide and attached to an XYZ micromanipulator, with the crystal facing the substrate (fixed on an XY axis movable stage). Since the stamp was transparent, the microscope could be used to find and align the $ReSe_2$ crystal to the identification markers on the substrate for it to bridge exactly the two neighboring GSCs. The stamp was lowered to get in touch with the substrate and gently pressed with a cotton swab. This allows an optimal contact between stamp and substrate, making sure that no air bubbles are trapped beneath the crystal. Finally, the stamp was slowly raised using the micromanipulator while monitoring the peeling process with the microscope. Images with an optical microscope were taken and used as a template for the Au contacts' mask drawing to have pads accessible to conventional tips for the electrical measurements. The substrate was spin-coated with

AZ 1505 photoresist (Microchemicals, Ulm, Germany) and then soaked on a 4:3 aqueous TMAH-based solution (AR 300-47, Allresist GmbH, Strausberg, Germany). This process induces partial insolubilization of the photoresist surface. It creates an overhang after exposure with laser lithography (DWL 2000, Heidelberg Instruments, Woburn, MA, USA) and development (AZ 400K developer 1:4, AZ Electronic Materials USA Corp., Somerville, NJ, USA) that ensures good metallic contact profiles and an effective lift-off process. A 3/50 nm thick Cr/Au layer was sputtered with a Kenosistec UHV sputtering tool and the metallic layer was removed (lift-off) by a room temperature acetone bath overnight. The entire device fabrication process schematic is shown in Figure 1.

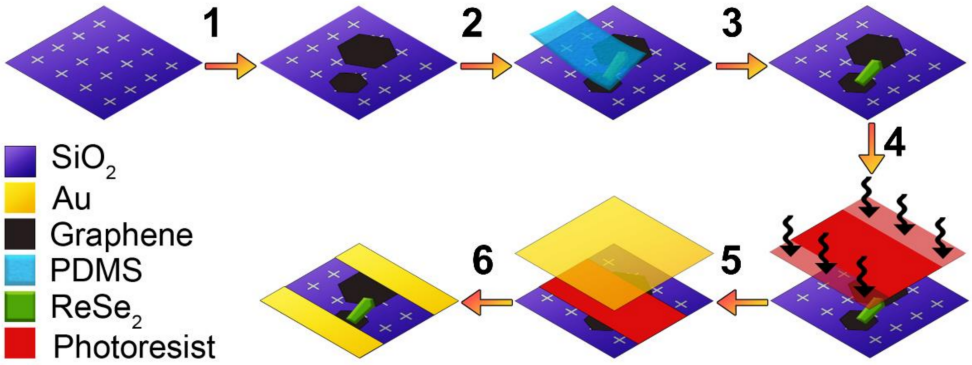

Figure 1. Schematic of the GSC/$ReSe_2$ device production process: (1) transfer of GSC to a Si/SiO_2 substrate with crosshair markers, (2–3) placement of the exfoliated ReSe2 crystal across two discrete GSCs by "pick & place" method, using a PDMS stamp, (4) spin-coating of photoresist and exposure with laser lithography to form the mask for the metallic contacts, (5) Cr/Au layers sputtering, and (6) partial removal of the metallic layer (lift-off) to form the Cr/Au contacts.

An analogous Au/$ReSe_2$ device was fabricated to compare the performance of graphene and Au contacts. A total of 3/50 nm Cr/Au contacts were sputtered onto a Si/SiO_2 (without markers) by the same process as explained above to form two 400-µm-wide electrodes with a 3-µm-gap separating them. Subsequently, an exfoliated $ReSe_2$ was transferred to bridge the two Au contacts by the "pick & place" method.

An hBN/GSC/$ReSe_2$ lateral-heterostructure device including a CVD hBN passivation layer was also fabricated to test our geometry with a thicker $ReSe_2$ crystal. The hBN film (4 nm thick) was transferred onto a Si/SiO_2 substrate (without markers) to act as a 2D passivation layer and a substrate for graphene. GSCs were transferred onto the Si/SiO_2/hBN substrate. Two GSCs with lateral sizes of ~250 µm and ~510 µm, spaced by 135 µm were identified at the microscope. A $ReSe_2$ crystal (600-nm-thick) was picked and placed across the two GSCs establishing a channel. The Cr/Au electrodes were fabricated by sputtering via a 125-µm-thick glass hard mask. The device fabrication process is schematically shown in Figure 2.

2.3. Raman Spectroscopy

Measurements were carried out on an ALPHA300 R Confocal Raman Microscope (WITec) using 532 nm laser light for excitation in the backscattering geometry at room temperature (the laser beam was focused on the sample by a 100× lens–Zeiss). The mapping measurements were performed using a 600 groove/mm grating with P_{Laser} = 0.8 mW, 4 s acquisition time and a 0.5 µm/point resolution. Using the WITec Suite FIVE software and the TrueComponentes analysis tool, three different spectra corresponding to each component-SiO_2 substrate, $ReSe_2$, and GSC-were selected and automatically color-coded.

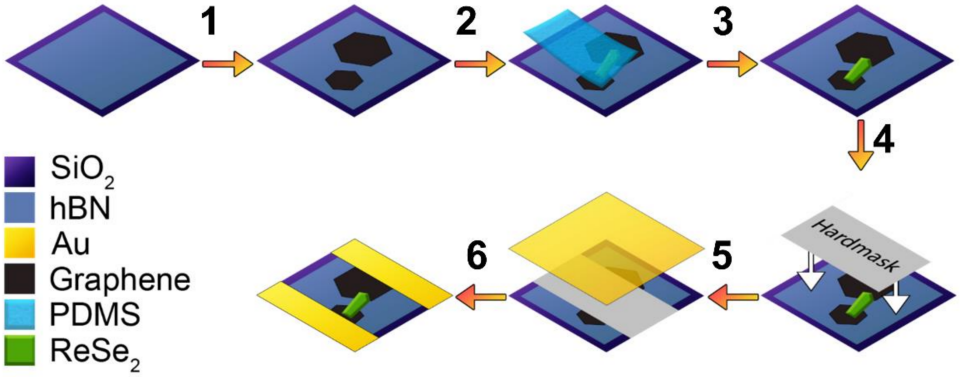

Figure 2. Schematic of the hBN/GSC/$ReSe_2$ device production process: (1) transfer of GSC to a Si/SiO_2/hBN substrate, (2–3) placement of the exfoliated $ReSe_2$ crystal across two discrete GSCs by "pick & place" method, using a PDMS stamp, (4) placement of a glass shadow mask (125-µm-thick) to form the mask for the metallic contacts, (5) Cr/Au layers sputtering, and (6) removal of the hard mask to form the Cr/Au contacts.

2.4. Atomic Force Microscopy (AFM)

Bruker Dimension ICON in tapping-mode was used with NANOSENSORS™ PPP-NCH tips with an average tip radius of curvature <10 nm, force constant of 10–130 N/m, and a 258.12 kHz resonance frequency. Image analysis was performed with Gwyddion software. To calculate the active area of the devices, S, only the region of the $ReSe_2$ flakes in between the contacts was selected.

2.5. Kelvin Probe Force Microscopy (KPFM)

Kelvin probe force microscopy (KPFM) experiments were performed in the same Bruker Dimension Icon AFM operated in air, using the amplitude modulation mode. For the dual-pass method, the lift height was set to 10 nm. We used Pt/Ir coated cantilevers (PPP-EFM Nanosensors, Neuchatel, Switzerland) with a nominal tip radius of 25 nm, a spring constant of 2.8 N/m, and 75 kHz resonance frequency. The tips were calibrated using a Au-coated Si sample for comparability of results. The contact potential difference (CPD) is defined as $V_{CPD} = e(\Phi_{tip} - \Phi_{sample})$, where Φ is the work function.

2.6. Electrical Measurements

The Seebeck coefficient of the $ReSe_2$ flake semiconductor on Au contacts was measured by heating the positive contact while keeping the negative contact at room temperature. Electrical properties of all three types of devices (Au/$ReSe_2$, GSC/$ReSe_2$ and hBN/GSC/$ReSe_2$) were measured with a source meter (Keithley 6470, Keithley Instruments, Solon, OH, USA) under ambient conditions. A different Au/$ReSe_2$ device from the KPFM measurements was used for electrical characterization, but its structure and contacts are the same, while having a similar $ReSe_2$ flake thickness within the same bulk regime (58 nm). For both the Au and the GSC devices I-V curves were acquired in the dark and under white light illumination for voltages between −2 and 2 V. The devices were also measured under 530 and 790 nm illumination and applied bias $V_{bias} = 2$ V, in order to calculate the responsivity and external quantum efficiency (EQE). The photoconductivity was measured as a function of the incident optical power by filtering the incident light beam with different neutral density filters. As for the hBN/GSC/$ReSe_2$ device, decay measurements were performed at increasing bias voltage: 50, 80, and 100 V. A 250 W halogen lamp with a spot size of 30 µm in diameter delivering an optical power of 962 W/m^2 was used. An external bias voltage of $V_{bias} = 50$ V applied between contacts was used for all the experiments under illumination.

3. Results

As a first step, we optimized the CVD process to produce sub-mm GSCs used as device contacts. The Cu substrates were pre-oxidized to partially passivate the Cu surface and decrease the graphene nucleation sites [36]. The pre-oxidation also enables the progressive release of a stable oxygen supply from the substrate during the high-temperature growth (1040 °C) and increases the crystal growth rate. The sapphire cavity also releases trace amounts of oxygen that stabilize the Cu oxidation level, compensating for the reduction of Cu-O bonds by atomic hydrogen. The graphite box mimics the Cu-enclosed configurations reported in the literature [37], by increasing the Cu vapor pressure inside the cavity and thus reducing the substrate roughness (due to continuous Cu re-deposition). By this approach, we could control the GSC size from 50 µm to a few millimeters. By keeping the initial seed concentration low and tuning the deposition time, the GSCs do not coalesce and can grow to sub-mm sizes and beyond, as shown in Figure 3a. For the larger crystals, the graphene nucleation density was as low as <600 nuclei/cm^2. Unlike the Cu-enclosed configuration, our approach does not damage the catalyst substrate and allows upscaling graphene growth on flat Cu foils of arbitrary size. After the transfer to a SiO_2 substrate (Figure 3b), two GSCs of ~0.25 mm^2 size separated by a small gap of ~5 µm were identified. As detailed in the Section 2.2, the GSC/$ReSe_2$ photodetector device studied in this work is a two-terminal photoresistor with in-plane current flowing via a $ReSe_2$ channel across two GSC contacts (acting as source and drain). The device is depicted conceptually in Figure 3c and shown in Figure 3d.

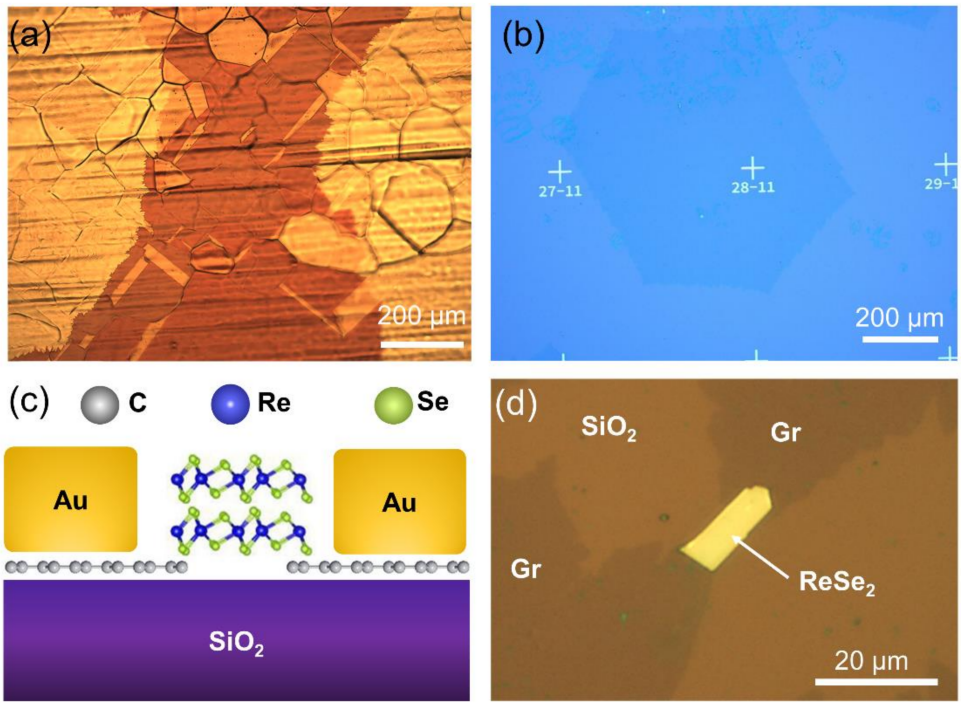

Figure 3. (**a**) GSCs grown by CVD on Cu substrates, which was oxidized after growth to enhance the contrast between GSC and substrate (**b**) The GSCs were transferred onto Si/SiO_2 wafer. (**c**) Schematic side-view and (**d**) optical top-view image of the GSC/$ReSe_2$ photodetector device. The $ReSe_2$ channel has ~5 µm width.

Raman spectroscopy was performed to evaluate the quality and structural properties of the 2D materials. The Raman spectra collected on the $ReSe_2$ crystal show an intricate signature in the 100–300 cm^{-1} range, with 13 first-order Raman active modes. This complex spectrum is attributed to the low crystal symmetry of Re-based dichalcogenides (associated with fundamental modes coupled to each other) and acoustic phonons [10]. Two prominent peaks at ~125 and ~160 cm^{-1} (Figure 4a), assigned to E_g-like and A_g-like modes,

respectively [14], were chosen to probe the anisotropic crystalline structure of $ReSe_2$ and study the dependence of the Raman modes to the laser light angle (by rotating the sample between 0–360°) [14,38]. Figure 4a shows that the E_g-like (125 cm^{-1}) and A_g-like (160 cm^{-1}) mode intensities strongly depend on the rotation angles, confirming the anisotropy of the $ReSe_2$ structure. The integrated intensities of these two modes are plotted in Figure 4b and are in line with previous studies [14]. The *b*-axis of the $ReSe_2$ lattice, which is along the Re_4 chains in the crystal, is parallel to the longer axis (dashed blue line in Figure 4b), connecting the two E_g-like mode maximum intensity points. Figure 4c shows the Raman spectra of Si/SiO_2, graphene, and $ReSe_2$ separately. In the Si/SiO_2 spectrum, the usual peak at 521 cm^{-1} due to the Si (001) substrate dominates. The I_{2D}/I_G ratio for graphene, the minimal D band, and a sharp symmetric 2D peak indicate high-quality defect-free single-layer graphene [39–42]. This is further supported by the 2D peak analysis, reporting a single and sharp (FWHM~31.9 cm^{-1}) Lorentzian band centered at ~2686.5 cm^{-1} [39,43]. Figure 4d shows a color-coded Raman map of the device, build with the spectra shown in 4c. Each pixel in the image stores one full Raman spectrum, and it is colored according to its similarity to one or more spectra in Figure 4c. All the images are consistent and give an accurate surface description based on the chemical composition of the area mapped.

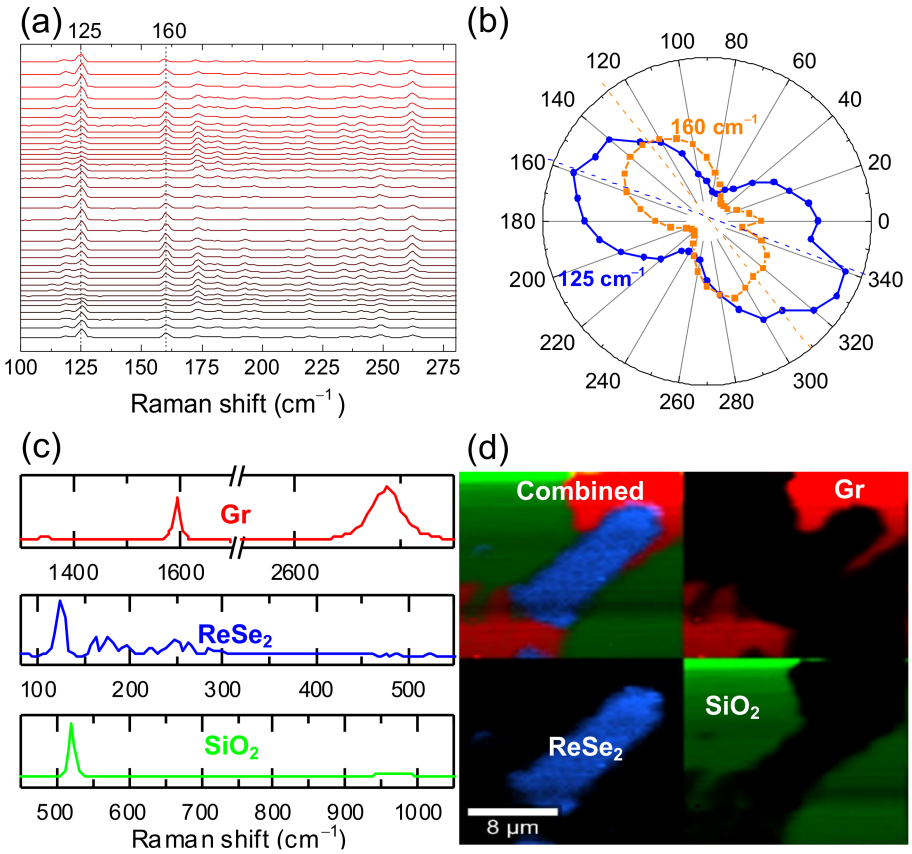

Figure 4. (**a**) Incident light polarization-dependent Raman spectra, obtained by rotating the sample from 0° to 360° (with a step of 10°) and the initial angle being arbitrary to the sample crystallographic axis. The peaks at 125 cm^{-1} and 160 cm^{-1} are strongly related to the rotation sample angles. (**b**) A plot of intensities of the two modes (125 cm^{-1} mode in dark blue and 160 cm^{-1} mode in orange). (**c**) Raman spectra representative of $ReSe_2$ (blue line), graphene (red line) and SiO_2 (green line). (**d**) Color-coded Raman map of the device, combining SiO_2 (green), GSC (red), and $ReSe_2$ (blue) Raman spectra. The Raman spectra presented in (**a**) were used as a reference to obtain the Raman mapping images.

Kelvin probe force microscopy measurements were conducted to evaluate the SBH between $ReSe_2$ and two different sets of metallic contacts, namely graphene and Au. Topog-

raphy and work function maps are shown in Figure 5a–d. For the GSC/$ReSe_2$ device, the profiles in Figure 5e indicate a thickness of ~95 nm and a work function $\Phi \approx 4.92 \pm 0.02$ eV for the $ReSe_2$ crystal, in good agreement with previously reported values [44]. The SBH_{GSC} was calculated from the work function difference between GSC contact and $ReSe_2$ considering the average of several profiles measured, obtaining $SBH_{GSC} \approx 0.06$ eV [45]. For the Au/$ReSe_2$ device, the $ReSe_2$ has a thickness ~180 nm and a work function $\Phi \approx 5.25 \pm 0.02$ eV (Figure 5f), giving $SBH_{Au} \approx 0.15$ eV.

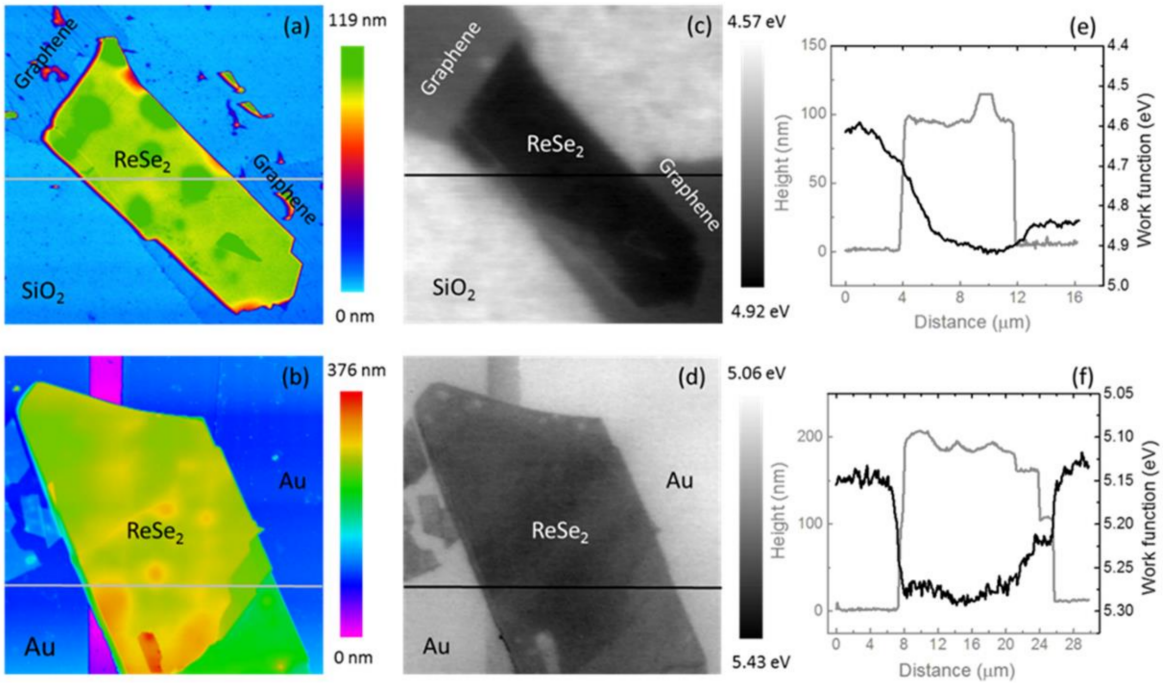

Figure 5. KPFM characterization of $ReSe_2$ devices. (**a**,**b**) Tapping mode topography (16.5 μm × 16.5 μm and 30 μm × 30 μm) of $ReSe_2$/graphene/SiO_2 and $ReSe_2$/Au. (**c**,**d**) Surface work function maps of the two devices. (**e**,**f**) Height and work function line profiles were obtained along the indicated gray and black solid lines. The right axis represents the absolute value of the work function.

The $ReSe_2$ flake Seebeck effect $\left(\alpha_n = -\frac{\Delta V}{\Delta T}\right)$ was measured [46], obtaining a negative Seebeck voltage, concluding that the semiconductor is n-type ($\alpha_n < 0$). The electrical characteristics were further studied to understand the device's transport mechanism, and the results are shown in Figure 6. Figure 6a compares the I-V curves of the GSC/$ReSe_2$ and Au/$ReSe_2$ devices in the dark. The GSC/$ReSe_2$ device presents consistently higher dark currents. Figure 6b shows a band diagram of GSC/$ReSe_2$ and Au/$ReSe_2$ contact junctions based on KPFM results. An equivalent circuit with two diodes connected in a back-to-back configuration with a series resistance (see Figure 6c inset) describes the Schottky barriers in the device. Figure 6c shows the I-V curves in the dark and under white light illumination. Figure 6d shows room temperature photocurrent values at V_{bias} = 2 V as a function of incident white light power by filtering the incident beam with neutral density filters of decreasing number, *ND*, from *ND* = 3.5 to 0 (no filter). Two different linear regimes were identified, one with a supralinear behavior (marked by a red line) and the other with an approximately linear trend (marked by a blue line).

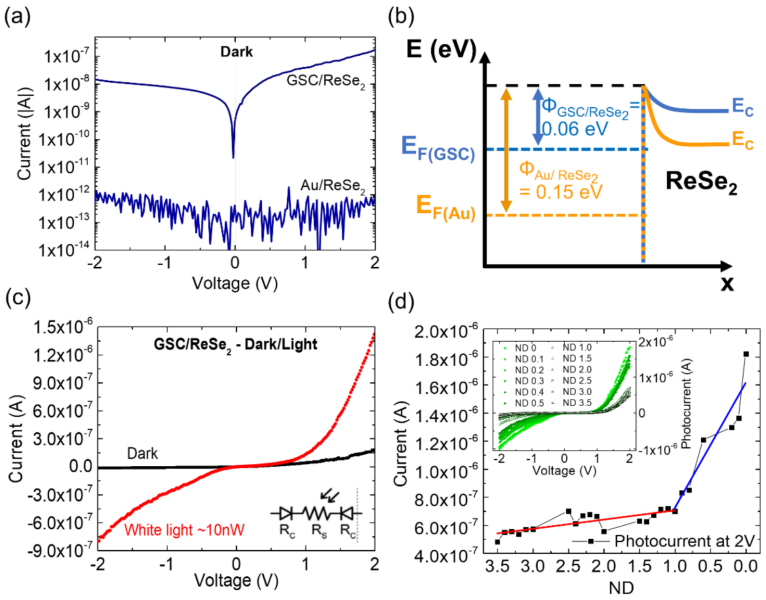

Figure 6. (**a**) I-V curves comparing GSC/$ReSe_2$ and Au/$ReSe_2$ devices without light illumination. (**b**) Band diagram of GSC/$ReSe_2$ and Au/$ReSe_2$ devices based on the KPFM results. (**c**) Dark and light I-V curves of the GSC/$ReSe_2$ device and the equivalent circuit with two Schottky barriers connected back-to-back with a series resistance (inset). (**d**) Response of the same device under white light and different attenuator filters (inset) and the corresponding current as a function of attenuator filters to an applied bias of 2 V highlighting the two different linear regimens (red and blue lines) with a transition point at ND~1.

The GSC/$ReSe_2$ device photocurrent ($I_{ph} = I_{light} - I_{dark}$) was measured under 530 nm and 790 nm wavelength illumination (Figure 7). It is worth noting that the measured photocurrent is the secondary photocurrent, which allows for a maximum gain greater than unity. The photocurrent increases with the incident illumination density, showing a power-law behavior $\left(I_{ph} \propto P^{\alpha_\lambda}\right)$, with exponent $\alpha_{530nm} = 0.44$ and $\alpha_{790nm} = 0.65$. At $V_{bias} = 2$ V, the photocurrent is ~0.4 µA and ~0.21 µA, respectively. The responsivity $\left(R_\lambda = \frac{I_{ph}}{P \times S}\right)$ and external quantum efficiency $\left(EQE = \frac{hcR_\lambda}{e\lambda}\right)$ were also calculated (P is the optical power density, S the active illuminated area of the device, being $S = 34\ \mu m^2$). The responsivity at maximum illumination power ($P_{530nm} = 2.8 \times 10^{-3}$ W·cm^{-2}, $P_{790nm} = 2.0 \times 10^{-3}$ W·cm^{-2} is $R_{530nm} = 4.7 \times 10^2$ A/W and $R_{790nm} = 3.3 \times 10^2$ A/W. In terms of EQE, the calculated values are $EQE_{530nm} = 1090\%$ and $EQE_{790nm} = 518\%$.

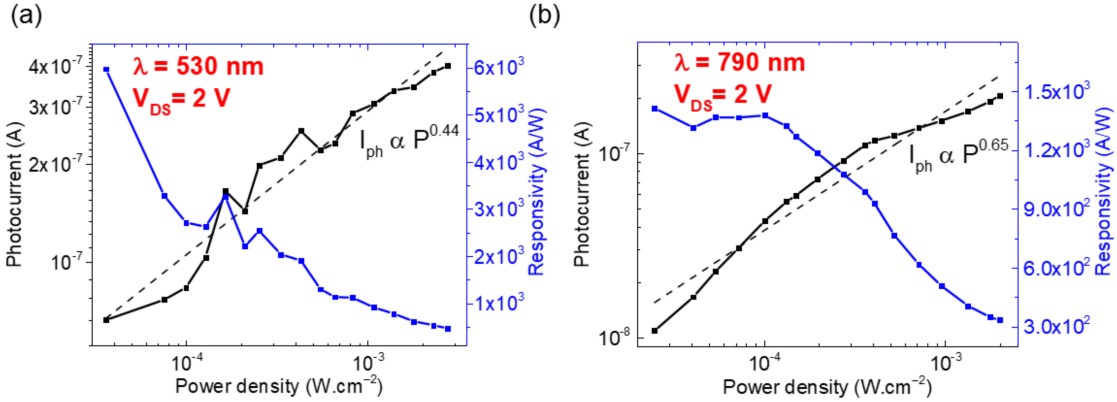

Figure 7. Photocurrent and responsivity as a function of irradiance under two different wavelengths exhibiting a P^α trend (**a**) 530 nm with a fit line for $\alpha = 0.44$ and (**b**) 790 nm with a fit line for $\alpha = 0.65$ for GSC/$ReSe_2$ device.

Another $ReSe_2$-based photodetector was fabricated by interfacing CVD-grown GSCs with an hBN passivation layer (see Section 2). For this device, a thicker $ReSe_2$ crystal (~600 nm) was exfoliated and selected to act as an absorbing layer, the purpose of testing the graphene contacts under much higher current levels. The schematic of the hBN/GSC/$ReSe_2$ device is depicted in Figure 8a, while an optical image is presented in Figure 8b. The materials were analyzed by Raman spectroscopy (Figure 8c), with results in line with the previous device: a 2D peak centered at ~2686.5 cm^{-1} for crystalline, monolayer graphene; two prominent peaks at ~125 and ~160 cm^{-1} for the mechanically exfoliated $ReSe_2$ crystal. The analysis of the CVD hBN confirms the expected E_{2g} peak at ~1372 cm^{-1}, corresponding to crystalline, few-layer hBN [47]. Photocurrent measurements (Figure 8d–f) were conducted on this hBN/GSC/$ReSe_2$ device. Figure 8d shows the time-resolved photoresponse obtained with a white light illumination through a chopper, with a high V_{bias} = 50 V to guarantee efficient photon absorption through most of the $ReSe_2$ thickness. The photocurrent oscillations follow the on/off cycles set by the chopper within the range of frequencies studied. The rise and decay times in each cycle were calculated by measuring the step time (Figure 8e), obtaining τ_{rise} = 0.5 s and τ_{decay} = 1.0 s. In Figure 8f, the photocurrent decay is recorded after turning off the light at t = 0 s, under the applied bias of V_{bias} = 50, 80 and 100 V. Each measurement under constant bias was repeated immediately after the first scan. The photocurrents show an exponential decay with a characteristic decay time τ_{decay} = 2.2 s, before reaching a steady-state value, which corresponds to the dark current. In order to compare the device performances, we calculated the photoconductivity under white light illumination ($\sigma_{ph} = \frac{I_{ph}}{A \times F}$, where I_{ph} is the measured photocurrent, A the cross-sectional area of the $ReSe_2$ flake and F the applied electric field—$F = \frac{V}{L}$, with V being the applied voltage and L the $ReSe_2$ flake length), as shown in Table 1.

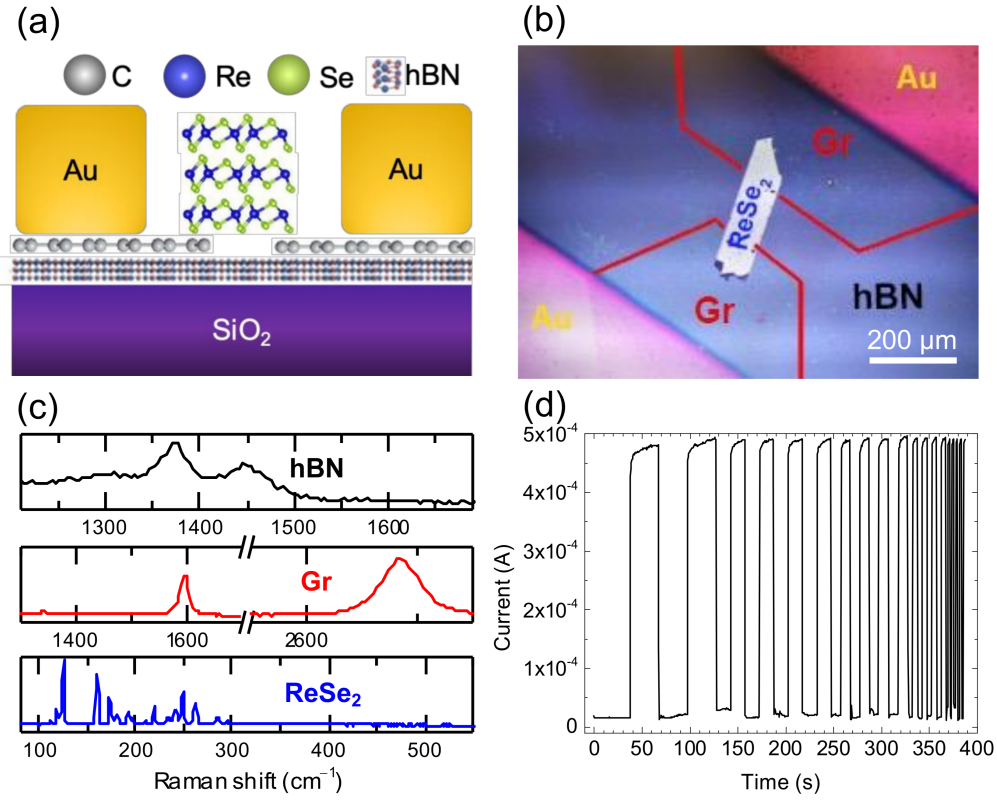

Figure 8. *Cont.*

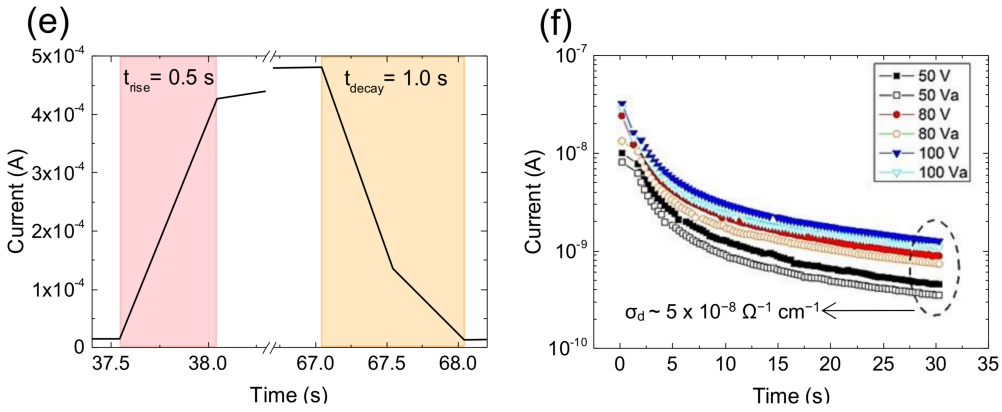

Figure 8. (**a**) Schematic side-view and (**b**) optical top-view image of the GSC/$ReSe_2$ device with the hBN passivation layer. (**c**) Raman spectra representative of hBN (black line), graphene (red line), and $ReSe_2$ (blue line). (**d**) Time response under illumination at V_{bias} = 50 V and (**e**) rise/decay time plot. (**f**) Photoresponse decay was performed at three increasing bias voltages: V_{bias} = 50, 80, 100 V. V_a is the second scan, obtained immediately after the first scan.

Table 1. Photodetector characteristics tested under white light illumination.

	Au/$ReSe_2$	**GSC/$ReSe_2$**	**hBN/GSC/$ReSe_2$**
I_{ph} (A)	4.5×10^{-10}	1.5×10^{-6}	4.6×10^{-4}
A (m^2)	4.9×10^{-13}	5.1×10^{-13}	5.2×10^{-11}
F (V/m)	6.7×10^{5}	3.2×10^{5}	3.6×10^{5}
σ_{ph} (S/m)	1.4×10^{-3}	9.2	24.7

As a first remark, the photoconductivity increases by three orders of magnitude when the GSC contacts are introduced. Notwithstanding the thicker $ReSe_2$ crystal, the hBN/GSC/$ReSe_2$ device photoconductivity is not so further increased, pointing at the low impact of the flake thickness on the overall device performance.

4. Discussion

The direct deposition of metallic contacts on atomic-thick materials (such as 2D TMDCs) can be detrimental, easily breaking in-plane covalent bonds and degrading the device performance [23]. By contrast, graphene provides advantages over standard metals in terms of formation of clean and defect-free interfaces through a non-damaging process [28,29]. Due to its very high thermal conductivity, graphene can also act as an excellent heat sink, reducing the chance of localized heat-induced damage to 2D semiconductors at high current densities, thus increasing the device's long-term stability [21]. When a metal contact is deposited on a semiconductor, a Schottky barrier may form depending on the metal's work function and the semiconductor electron/hole affinity [48]. In general, a sizable Schottky barrier height (SBH) leads to a rectifying contact that limits the current injection/extraction, as opposed to ohmic contacts (setting no barrier to the current flow) [25]. In 2D materials, the absence of dangling bonds on either side of the in-plane conduction path and the anisotropic charge carrier transport across the active region can give rise to very high contact resistance, due to large SBH or Fermi level pinning [49,50]. Thus, the appropriate material choice for low-dimensional contacts is essential to prevent or minimize the SBH [21,51]: metal/graphene/TMDC contacts showed ohmic-like behavior due to minimal SBH [52,53]. Furthermore, it is possible to tune the work function of graphene in 2D devices by external gating [54,55]. In our devices with back-to-back configuration, the reverse saturation current (I_s) of each diode (formed at the junctions between the two metal contacts and $ReSe_2$) exponentially decay with the Schottky barrier height (Φ_{SHB}), as follows:

$$I_s \propto \exp\left(-\frac{q\Phi_{SHB}}{k_B T}\right) \quad (1)$$

As shown in Figure 6a, the GSC/$ReSe_2$ dark current is ~160 nA (at 2V), in line with previous reports on undoped $ReSe_2$ devices, usually indicating low carrier density (~3×10^{13} cm^{-2} [56]). The $ReSe_2$ resistivity was 17 Ω·cm (close to ~5 Ω·cm reported in ref. [57]). The Au/$ReSe_2$ dark current was ~0.5 pA, i.e., 3.2×10^5 smaller than the graphene-contacted devices. The device dark currents can be thus easily explained by Equation (1), when considering the two Φ_{SHB} measured by KPFM (i.e., 0.06 eV for GSC, 0.15 eV for Au), as illustrated by the band diagrams in Figure 6b. The small electron barrier in the GSC/$ReSe_2$ device increases the probability of electron injection from the metal to the $ReSe_2$ film even at room temperature. In the GSC/$ReSe_2$ device under illumination, a marked increase in $ReSe_2$ conductivity was observed (Figure 6c). At low bias (V_{bias} < 1.5 V), the current limiting effect of the two Schottky barriers on the current is highlighted by the non-linear IV characteristic. For higher bias (~1.5 V < V_{bias} < 2 V), the contacts appeared as non-blocking, with the current showing linear behavior [58]. The room temperature measurements at V_{bias} = 2 V (Figure 6d) showed a photocurrent trend following two regimes: a supralinear behavior (marked by the red line) around a transition point, occurring at $ND > 1$, and an approximately linear trend (marked by the blue line) for $ND < 1$ (see also the inset). This behavior could be explained by a combination of effects due to sensitization and electronic doping. Increased doping can occur by increasing the light intensity, which generates higher photocarrier concentrations. Changing carrier concentration is equivalent to moving the steady-state pseudo-Fermi levels (E_{Fn} and E_{Fp}) across the semiconductor bandgap. This transformation occurring for $ND < 1$ and entirely changes the carrier transport as the localized states inside the bandgap change from traps to recombination centers as E_{Fn} (E_{Fp}) move up (down) in the semiconductor bandgap, scanning different defect bands [59].

The photocurrent ($I_{ph\ 530nm}$ = 0.4 μA, $I_{ph\ 790nm}$ = 0.21 μA) of our GSC/$ReSe_2$ device was one order of magnitude higher than those reported for similar $ReSe_2$ devices with metallic contacts (see Table 2). The photocurrent increases with the incident illumination density, showing a power-law behavior ($I_{ph} \propto P^{\alpha_\lambda}$) with α_{530nm} = 0.44 and α_{790nm} = 0.65. A value close to 1 indicates a photoconductive response, while $0 < \alpha_\lambda < 1$ indicates a dominant photogating behavior, as expected for low-dimensional photodetectors with very high exciton binding energy and reduced dielectric screening [60,61]. The calculated responsivity with maximum illumination power ($P_{530nm} = 2.8 \times 10^{-3}$ W.cm^{-2} and $P_{790nm} = 2.0 \times 10^{-3}$ W.cm^{-2}) is $R_{530nm} = 4.7 \times 10^2$ A/W and $R_{790nm} = 3.3 \times 10^2$ A/W are superior to the second device we fabricated with Au contacts (flake thickness of 58 nm and S = 26 μm^2) and to other works on exfoliated $ReSe_2$ devices. Furthermore, these values are similar to those obtained for a p-doped $ReSe_2$ device fabricated [62] (see Table 2). The secondary photocurrent measure depends on the majority carrier concentration or on the photocarrier with the higher mobility, μ. Therefore, it is possible to have gain, G, given by the ratio of photocarrier lifetime, τ_{ph}, to photocarrier transit time, τ_{tr} ($G = \tau_{ph}/\tau_{tr}$) [59]. Then, the calculated EQE values (EQE_{530nm} = 1090% and EQE_{790nm} = 518%) are >>100% and vastly superior to the Au/$ReSe_2$ device. These values confirm the non-blocking nature of the graphene contacts at the working bias, result in a photoconductive gain [59]. Such large EQE values may be due to a distribution of traps that decreases the lifetime of one carrier type while increasing the other's (i.e., sensitization), with the photoconductive gain being proportional to the lifetime of the photo-excited carriers [63,64]. To compare our GSC/$ReSe_2$ device with other reported works, Table 2 summarizes the parameters and performance of $ReSe_2$-based photodetectors. Recent progress in CVD-grown $ReSe_2$ devices [38,65] has shown a lower photo-responsivity (between ~3–8 A/W) compared to other devices with exfoliated crystals. Further, a wide range of mobility values is observed, from 9.8 to 1.36×10^{-3} cm^2/(V.s), primarily due to a variable density of grain boundaries in polycrystalline CVD samples. Similar works with exfoliated $ReSe_2$ devices with Au electrodes reported <100 nA photocurrents and lower responsivities [12,66], identical to the CVD-grown $ReSe_2$ devices.

Table 2. Comparison of key parameters from our $ReSe_2$+Gr device and other reported $ReSe_2$ based photodetectors.

Ref.	Photodetector	Thickness (nm)	Active Area, S (μm^2)	Incident λ (nm)	Incident Power	I_{ph}	R (A/W)	EQE (%)
Our work	Exfoliated $ReSe_2$ and Au electrodes on Si/SiO_2	58	26	530 790	3.3/2.9 mW cm^{-2}	$4.0/1.6 \times 10^{-11}$ (V_{bias} = 2 V)	4.7×10^{-2} 2.1×10^{-2}	11 3
Our work	Exfoliated $ReSe_2$ and Gr electrodes on Si/SiO_2	95	34	530 790	2.7/1.9 mW cm^{-2}	$4 \times 10^{-7}/2.1 \times 10^{-7}$ A (V_{bias} = 2 V)	4.7×10^{2} 3.3×10^{2}	1099 518
[67]	ML Gr/$ReSe_2$/ML Gr heterostructure on Si/SiO_2	14.5	18	220	0.14 mW cm^{-2}	4.5×10^{-5} A (V_{bias} = 5 V)	1.2×10^{6}	64
[38]	CVD $ReSe_2$ and Cr/Au electrodes on Si/SiO_2	4.2	5.8	808	5.7×10^{2} mW cm^{-2}	9.7×10^{-8} A (V_{bias} = 5 V)	2.98	458
[65]	CVD $ReSe_2$ and Cr/Au electrodes on Si/SiO_2	0.71	19	850 940	6.1/7.0 mW cm^{-2}	1×10^{-8} A/4×10^{-9} A (V_{bias} = 1 V)	8.4 5.1	12 7
[12]	Exfoliated $ReSe_2$ and Cr/Au electrodes on Si/SiO_2	0.66	4	633	1×10^{2} mW cm^{-2}	7.91×10^{-8} A (V_{bias} = 0.5 V)	17.8	3048
[66]	Exfoliated $ReSe_2$ and Cr/Au electrodes on Si/SiO_2	65	N/A	633	2.48 mW cm^{-2}	1×10^{-8} A (V_{bias} = 1 V)	2.22	4
[68]	Exfoliated $ReSe_2$ and Ti/Pd electrodes on Si/SiO_2	80	25	785	1 mW cm^{-2}	5.9×10^{-8} A (V_{bias} = 5 V)	4.3×10^{3}	6791
[44]	Exfoliated $ReSe_2$ and Ti electrodes on Si/SiO_2	50.4	25	405	1 nW	3.62×10^{-7} A μm^{-1} (V_{bias} = 5 V)	1.1×10^{3}	3367
[68]	Exfoliated $ReSe_2$ and Pt electrodes on Si/SiO_2	35	25	520	10 nW	1.61×10^{-7} A μm^{-1} (V_{bias} = 5 V)	79.99	191
[44]	Exfoliated $ReSe_2$ + $MoSe_2$ heterostructure and Cr/Au electrodes on Si/SiO_2	60	141	633	5.15 mW cm^{-2}	4.9×10^{-8} A (V_{bias} = 1 V)	6.75	1266
[62]	Exfoliated $ReSe_2$ p-doped with HCl and Pt electrodes on Si/SiO_2	35	25	520	10 nW	6.32×10^{-7} A μm^{-1} (V_{bias} = 5 V)	3.144×10^{2}	750
[69]	Exfoliated Mo:$ReSe_2$ and Cr/Au electrodes on Si/SiO_2	4.5	336	633	2×10^{1} mW cm^{-2}	2.2×10^{-6} A (V_{bias} = 1 V)	55.5	109
[70]	Exfoliated ReSSe and Ti/Au electrodes on Si/SiO_2	3	22	532	3.2 mW cm^{-2}	5×10^{-9} A μm^{-1} (V_{bias} = 5 V)	8	19

In electronic devices, graphene can be strongly influenced by the underlying substrate. Although still the ubiquitous choice, SiO_2 substrates for 2DMs may present several constraints related to roughness [71], charged impurities [30,72,73], and surface optical phonons [73,74]. Consequently, electron-hole charge fluctuations can originate in graphene on SiO_2, scattering charge carriers and hence limiting device performance [30,75]. Graphene can reach the highest electron mobility and show minimal carrier inhomogeneity when supported by hexagonal boron nitride (hBN) [32,76]. hBN's surface optical phonon modes have higher energies than similar modes in SiO_2, improving high-temperature and high-electric-field performance of hBN and graphene-based devices [77,78]. Moreover, the inclusion of an hBN layer in the device can reduce roughness, intrinsic doping, and chemical reactivity of the fabricated device [71]. Following this rationale, we tested the introduction of an hBN passivation layer onto SiO_2. For this device, a $ReSe_2$ flake with a higher thickness (600 nm, about $\times 6$ the previous one) was selected to demonstrate the thickness-independence of the $ReSe_2$ optoelectronic properties while maximizing the photon harvesting and increasing the signal-to-noise sensor output. Notice that photocurrent levels (Figure 8d,e) are approximately two orders of magnitude higher (I_{ph} ~10^{-4} A) than in the previous experiments (I_{ph} ~10^{-6} A), as expected for a thicker $ReSe_2$ absorbing layer and a higher applied voltage. Even so, the graphene-on-hBN contacts provided a sufficient current injection and collection able to sustain the photocurrent in all cases. In photoresponse decay measurements (Figure 8f), a steep current decay was observed. The decay time corresponds to the transient regimen between the two steady states—under illumination and in the dark—during which carriers de-trap and drift to the contacts under the applied field. The measured decay time, extracted from the fitting to an exponential profile, is τ_{decay} = 2.2 s in line with decay times found in the literature for this type of device [63]. The steady-state dark current is ~3×10^{-10} A, which gives a photo-to-dark current ratio of ~10^6, i.e., a value comparable with those found in the most photosensitive optoelectronic thin-film materials (e.g., a-Si:H, CdTe, CIGS, or $CH_3NH_3PbI_3$ perovskites). These findings show that the $ReSe_2$ multilayer crystals represent a solid choice for high-photosensitivity photodetectors.

5. Conclusions

A design for photodetector based on mechanically exfoliated $ReSe_2$ crystal and GSC contacts in a lateral-heterostructure design was proposed. The device fabrication started with the growth of 200-µm-wide GSCs by CVD on Cu foil followed by transfer to a Si/SiO_2 substrate. A ~100 nm-thick $ReSe_2$ crystal was exfoliated and placed across two GSCs contacts by the "pick & place" method. This fabrication technique provides a simple and effective way to optically identify the desired atomically thin crystals amongst the high range of exfoliated flakes' sizes and thicknesses while precisely controlling their orientation and position. Furthermore, since it is an all-dry procedure, it is possible to minimize the amount of additional contaminations. To compare the performance of GSC and Au contacts, a $Au/ReSe_2$ photodetector was fabricated using the same crystal exfoliation and "pick & place" transfer methods. Owing to a low SBH with the $ReSe_2$ crystal for the GSC (SBH $\approx$ 0.06 eV, as opposed to SBH $\approx$ 0.15 eV for the Au contacts), higher currents were measured in GSC-contacted devices in both the dark and illuminated which resulted in a higher gain and an enhanced linearity. The $GSC/ReSe_2$ dark current was about 2×10^4 higher than that of the $Au/ReSe_2$ device. The $GSC/ReSe_2$ photocurrent was one order of magnitude higher than similar $ReSe_2$-based devices with metallic contacts reported in the literature. The responsivity, $R_{530nm} = 4.7 \times 10^2$ A/W and $R_{790nm} = 3.3 \times 10^2$ A/W was higher than in other reported devices. The external quantum efficiency under bias is in the expected range for this type of device with EQE_{530nm} = 1090% and EQE_{790nm} = 518%, confirming the non-blocking nature of the graphene contacts at V_{bias} = 2 V. Lastly, by implementing a CVD hBN passivation layer, an $hBN/GSC/ReSe_2$ photodetector was fabricated. A $ReSe_2$ crystal with a greater thickness was chosen to (i) maximize photon harvesting and (ii) study recombination effects of $ReSe_2$. Under white light illumination, the $hBN/GSC/ReSe_2$ device's electrical response was characterized by a rise time of 0.5 s,

coherent with the on/off cycles. The electrical conductivity as a function of the optical power saturated at ~10^3 W/m, with a photo-to-dark current ratio of ~10^6, a value that proofs $ReSe_2$'s adequacy as an absorbing layer in photodetectors.

Author Contributions: Conceptualization, P.A., A.C.; methodology, P.A.; validation, A.C.; formal analysis, B.S. (Bruna Silva); investigation, J.R., B.S. (Balaji Sompalle), C.-D.L., N.N., J.B., F.C., M.C.; resources, P.A.; data curation, B.S. (Bruna Silva), J.R., N.N., J.B., F.C., M.C., S.S., P.A., A.C.; writing—original draft preparation, J.R.; writing—review and editing, B.S. (Bruna Silva), S.S., P.A., A.C.; supervision, A.C.; project administration, A.C.; funding acquisition, P.A., A.C. All authors have read and agreed to the published version of the manuscript.

Funding: This research was funded by National Funds through the Portuguese Foundation for Science and Technology (FCT) in the framework of the Strategic Funding UIDB/04650/2020 and projects PTDC/FIS-NAN/3668/2014 (LA2D) and PTDC/FIS-MAC/28114/2017 (POCI-01-0145-FEDER-028114) (GRAPHSENS). A.C. acknowledges the financial support of the project "GEMIS–Graphene-enhanced Electro-Magnetic Interference Shielding," with the reference POCI-01-0247-FEDER-045939, co-funded by COMPETE 2020–Operational Programme for Competitiveness and Internationalization and FCT–Science and Technology Foundation, under the Portugal 2020 Partnership Agreement, through the European Regional Development Fund (ERDF).

Institutional Review Board Statement: Not applicable.

Informed Consent Statement: Not applicable.

Data Availability Statement: Not applicable.

Acknowledgments: We acknowledge the kind support by Martin Pumera, who supplied the $ReSe_2$ bulk crystals.

Conflicts of Interest: The authors declare no conflict of interest. The funders had no role in the design of the study; in the collection, analyses, or interpretation of data; in the writing of the manuscript, or in the decision to publish the results.

References

1. Manzeli, S.; Ovchinnikov, D.; Pasquier, D.; Yazyev, O.V.; Kis, A. 2D Transition Metal Dichalcogenides. *Nat. Rev. Mater.* **2017**, *2*, 1–15. [CrossRef]
2. Jung, Y.; Ji, E.; Capasso, A.; Lee, G.-H. Recent Progresses in the Growth of Two-Dimensional Transition Metal Dichalcogenides. *J. Korean Ceram. Soc.* **2019**, *56*, 24–36. [CrossRef]
3. Wang, Q.H.; Kalantar-Zadeh, K.; Kis, A.; Coleman, J.N.; Strano, M.S.; Kis, A.; Coleman, J.N.; Wang, Q.H.; Kalantar-Zadeh, K. Electronics and Optoelectronics of Two-Dimensional Transition Metal Dichalcogenides. *Nat. Nanotechnol.* **2012**, *7*, 699–712. [CrossRef] [PubMed]
4. Mak, K.F.; Shan, J. Photonics and Optoelectronics of 2D Semiconductor Transition Metal Dichalcogenides. *Nat. Photonics* **2016**, *10*, 216–226. [CrossRef]
5. Choi, W.; Choudhary, N.; Han, G.H.; Park, J.; Akinwande, D.; Lee, Y.H. Recent Development of Two-Dimensional Transition Metal Dichalcogenides and Their Applications. *Mater. Today* **2017**, *20*, 116–130. [CrossRef]
6. Ahmed, S.; Yi, J. Two-Dimensional Transition Metal Dichalcogenides and Their Charge Carrier Mobilities in Field-Effect Transistors. *Nano Micro Lett.* **2017**, *9*, 1–23. [CrossRef]
7. Kang, S.; Lee, D.; Kim, J.; Capasso, A.; Kang, H.S.; Park, J.W.; Lee, C.H.; Lee, G.H. 2D Semiconducting Materials for Electronic and Optoelectronic Applications: Potential and Challenge. *2D Mater.* **2020**, *7*, 022003. [CrossRef]
8. Yu, Z.G.; Cai, Y.; Zhang, Y.W. Robust Direct Bandgap Characteristics of One-and Two-Dimensional ReS 2. *Sci. Rep.* **2015**, *5*, 1–9.
9. Jariwala, B.; Voiry, D.; Jindal, A.; Chalke, B.A.; Bapat, R.; Thamizhavel, A.; Chhowalla, M.; Deshmukh, M.; Bhattacharya, A. Synthesis and Characterization of ReS2 and ReSe2 Layered Chalcogenide Single Crystals. *Chem. Mater.* **2016**, *28*, 3352–3359. [CrossRef]
10. Tongay, S.; Sahin, H.; Ko, C.; Luce, A.; Fan, W.; Liu, K.; Zhou, J.; Huang, Y.S.; Ho, C.H.; Yan, J.; et al. Monolayer Behaviour in Bulk ReS 2 Due to Electronic and Vibrational Decoupling. *Nat. Commun.* **2014**, *5*, 1–6. [CrossRef]
11. Chenet, D.A.; Aslan, O.B.; Huang, P.Y.; Fan, C.; Van Der Zande, A.M.; Heinz, T.F.; Hone, J.C. In-Plane Anisotropy in Mono- and Few-Layer ReS2 Probed by Raman Spectroscopy and Scanning Transmission Electron Microscopy. *Nano Lett.* **2015**, *15*, 5667–5672. [CrossRef]
12. Yang, S.; Tongay, S.; Li, Y.; Yue, Q.; Xia, J.B.; Li, S.S.; Li, J.; Wei, S.H. Layer-Dependent Electrical and Optoelectronic Responses of ReSe2 Nanosheet Transistors. *Nanoscale* **2014**, *6*, 7226–7231. [CrossRef]

13. Aslan, O.B.; Chenet, D.A.; Van Der Zande, A.M.; Hone, J.C.; Heinz, T.F. Linearly Polarized Excitons in Single- and Few-Layer ReS2 Crystals. *ACS Photonics* **2016**, *3*, 96–101. [CrossRef]
14. Wolverson, D.; Crampin, S.; Kazemi, A.S.; Ilie, A.; Bending, S.J. Raman Spectra of Monolayer, Few-Layer, and Bulk ReSe2: An Anisotropic Layered Semiconductor. *ACS Nano* **2014**, *8*, 11154–11164. [CrossRef]
15. Zhang, E.; Jin, Y.; Yuan, X.; Wang, W.; Zhang, C.; Tang, L.; Liu, S.; Zhou, P.; Hu, W.; Xiu, F. ReS2-Based Field-Effect Transistors and Photodetectors. *Adv. Funct. Mater.* **2015**, *25*, 4076–4082. [CrossRef]
16. Xu, K.; Deng, H.X.; Wang, Z.; Huang, Y.; Wang, F.; Li, S.S.; Luo, J.W.; He, J. Sulfur Vacancy Activated Field Effect Transistors Based on ReS2 Nanosheets. *Nanoscale* **2015**, *7*, 15757–15762. [CrossRef]
17. Dathbun, A.; Kim, Y.; Kim, S.; Yoo, Y.; Kang, M.S.; Lee, C.; Cho, J.H. Large-Area CVD-Grown Sub-2 V ReS2 Transistors and Logic Gates. *Nano Lett.* **2017**, *17*, 2999–3005. [CrossRef] [PubMed]
18. Park, J.Y.; Joe, H.E.; Yoon, H.S.; Yoo, S.; Kim, T.; Kang, K.; Min, B.K.; Jun, S.C. Contact Effect of ReS2/Metal Interface. *ACS Appl. Mater. Interfaces* **2017**, *9*, 26325–26332. [CrossRef]
19. Shim, J.; Oh, A.; Kang, D.H.; Oh, S.; Jang, S.K.; Jeon, J.; Jeon, M.H.; Kim, M.; Choi, C.; Lee, J.; et al. Thin-Film Transistors: High-Performance 2D Rhenium Disulfide (ReS2) Transistors and Photodetectors by Oxygen Plasma Treatment (Adv. Mater. 32/2016). *Adv. Mater.* **2016**, *28*, 6984. [CrossRef]
20. Castellanos-Gomez, A.; Vicarelli, L.; Prada, E.; Gacem, K.; Boukhicha, M.; Chen, Z.; Uwanno, T.; Hattori, Y.; Taniguchi, T.; Ferraz Da Costa, M.C.; et al. Deterministic Transfer of Two-Dimensional Materials by All-Dry Viscoelastic Stamping. *2D Mater.* **2014**, *1*, 011002. [CrossRef]
21. Allain, A.; Kang, J.; Banerjee, K.; Kis, A. Electrical Contacts to Two-Dimensional Semiconductors. *Nat. Mater.* **2015**, *14*, 1195–1205. [CrossRef] [PubMed]
22. Hu, Z.; Wu, Z.; Han, C.; He, J.; Ni, Z.; Chen, W. Two-Dimensional Transition Metal Dichalcogenides: Interface and Defect Engineering. *Chem. Soc. Rev.* **2018**, *47*, 3100–3128. [CrossRef] [PubMed]
23. Schulman, D.S.; Arnold, A.J.; Das, S. Contact Engineering for 2D Materials and Devices. *Chem. Soc. Rev.* **2018**, *47*, 3037–3058. [CrossRef]
24. Dhahi, T.S.; Ahmad, S. Metal Contacts to 2d-Materials for Device Applications. *Electr. Electron. Technol. Open Access J.* **2018**, *2*, 31–38.
25. Rhoderick, E.H. Metal-Semiconductor Contacts. *IEE Proc. I Solid State Electron Devices* **1982**, *129*, 1–14. [CrossRef]
26. Novoselov, K.S.; Mishchenko, A.; Carvalho, A.; Castro Neto, A.H.; Neto, A.H.C.; Castro Neto, A.H.; Neto, A.H.C. 2D Materials and van Der Waals Heterostructures. *Science* **2016**, *353*, aac9439. [CrossRef]
27. Wang, L.; Meric, I.; Huang, P.Y.; Gao, Q.; Gao, Y.; Tran, H.; Taniguchi, T.; Watanabe, K.; Campos, L.M.; Muller, D.A.; et al. One-Dimensional Electrical Contact to a Two-Dimensional Material. *Science* **2013**, *342*, 614–617. [CrossRef]
28. Giubileo, F.; Di Bartolomeo, A. The Role of Contact Resistance in Graphene Field-Effect Devices. *Prog. Surf. Sci.* **2017**, *92*, 143–175. [CrossRef]
29. Das, S.; Chen, H.Y.; Penumatcha, A.V.; Appenzeller, J. High Performance Multilayer MoS2 Transistors with Scandium Contacts. *Nano Lett.* **2013**, *13*, 100–105. [CrossRef]
30. Watanabe, K.; Taniguchi, T.; Kanda, H. Direct-Bandgap Properties and Evidence for Ultraviolet Lasing of Hexagonal Boron Nitride Single Crystal. *Nat. Mater.* **2004**, *3*, 404–409. [CrossRef]
31. Giovannetti, G.; Khomyakov, P.A.; Brocks, G.; Kelly, P.J.; Van Den Brink, J. Substrate-Induced Band Gap in Graphene on Hexagonal Boron Nitride: Ab Initio Density Functional Calculations. *Phys. Rev. B Condens. Matter Mater. Phys.* **2007**, *76*, 073103. [CrossRef]
32. Dean, C.R.; Young, A.F.; Meric, I.; Lee, C.; Wang, L.; Sorgenfrei, S.; Watanabe, K.; Taniguchi, T.; Kim, P.; Shepard, K.L.; et al. Boron Nitride Substrates for High-Quality Graphene Electronics. *Nat. Nanotechnol.* **2010**, *5*, 722–726. [CrossRef] [PubMed]
33. Geim, A.K.; Novoselov, K.S. The Rise of Graphene. *Nat. Mater.* **2007**, *6*, 183–191. [CrossRef] [PubMed]
34. Cabral, P.D.; Domingues, T.; Machado, G.; Chicharo, A.; Cerqueira, F.; Fernandes, E.; Athayde, E.; Alpuim, P.; Borme, J. Clean-Room Lithographical Processes for the Fabrication of Graphene Biosensors. *Materials (Basel)* **2020**, *13*, 5728. [CrossRef]
35. Sofer, Z.; Sedmidubský, D.; Luxa, J.; Bouša, D.; Huber, Š.; Lazar, P.; Veselý, M.; Pumera, M. Universal Method for Large-Scale Synthesis of Layered Transition Metal Dichalcogenides. *Chem. Eur. J.* **2017**, *23*, 10177–10186. [CrossRef]
36. Gnisci, A.; Faggio, G.; Messina, G.; Kwon, J.; Lee, J.-Y.; Lee, G.-H.; Dikonimos, T.; Lisi, N.; Capasso, A. Ethanol-CVD Growth of Sub-Mm Single-Crystal Graphene on Flat Cu Surfaces. *J. Phys. Chem. C* **2018**, *122*. [CrossRef]
37. Li, X.; Magnuson, C.W.; Venugopal, A.; Tromp, R.M.; Hannon, J.B.; Vogel, E.M.; Colombo, L.; Ruoff, R.S. Large-Area Graphene Single Crystals Grown by Low-Pressure Chemical Vapor Deposition of Methane on Copper. *J. Am. Chem. Soc.* **2011**, *133*, 2816–2819. [CrossRef] [PubMed]
38. Hafeez, M.; Gan, L.; Li, H.; Ma, Y.; Zhai, T. Chemical Vapor Deposition Synthesis of Ultrathin Hexagonal ReSe $_2$ Flakes for Anisotropic Raman Property and Optoelectronic Application. *Adv. Mater.* **2016**, *28*, 8296–8301. [CrossRef] [PubMed]
39. Ferrari, A.C.; Basko, D.M. Raman Spectroscopy as a Versatile Tool for Studying the Properties of Graphene. *Nat. Nanotechnol.* **2013**, *8*, 235–246. [CrossRef] [PubMed]
40. Capasso, A.; Dikonimos, T.; Sarto, F.; Tamburrano, A.; De Bellis, G.; Sarto, M.S.M.S.; Faggio, G.; Malara, A.; Messina, G.; Lisi, N. Nitrogen-Doped Graphene Films from Chemical Vapor Deposition of Pyridine: Influence of Process Parameters on the Electrical and Optical Properties. *Beilstein J. Nanotechnol.* **2015**, *6*, 2028–2038. [CrossRef]

41. Faggio, G.; Capasso, A.; Messina, G.; Santangelo, S.; Dikonimos, T.; Gagliardi, S.; Giorgi, R.; Morandi, V.; Ortolani, L.; Lisi, N. High-Temperature Growth of Graphene Films on Copper Foils by Ethanol Chemical Vapor Deposition. *J. Phys. Chem. C* **2013**, *117*, 21569–21576. [CrossRef]
42. Faggio, G.; Messina, G.; Lofaro, C.; Lisi, N.; Capasso, A. Recent Advancements on the CVD of Graphene on Copper from Ethanol Vapor. *C J. Carbon Res.* **2020**, *6*, 14. [CrossRef]
43. Capasso, A.; Bellani, S.; Palma, A.L.; Najafi, L.; Del Rio Castillo, A.E.; Curreli, N.; Cina, L.; Miseikis, V.; Coletti, C.; Calogero, G.; et al. CVD-Graphene/Graphene Flakes Dual-Films as Advanced DSSC Counter Electrodes. *2D Mater.* **2019**, *6*, 035007. [CrossRef]
44. Jo, S.H.; Lee, H.W.; Shim, J.; Heo, K.; Kim, M.; Song, Y.J.; Park, J.H. Highly Efficient Infrared Photodetection in a Gate-Controllable Van Der Waals Heterojunction with Staggered Bandgap Alignment. *Adv. Sci.* **2018**, *5*, 1–9. [CrossRef]
45. Capasso, A.; Salamandra, L.; Faggio, G.; Dikonimos, T.; Buonocore, F.; Morandi, V.; Ortolani, L.; Lisi, N. Chemical Vapor Deposited Graphene-Based Derivative As High-Performance Hole Transport Material for Organic Photovoltaics. *ACS Appl. Mater. Interfaces* **2016**, *8*, 23844–23853. [CrossRef]
46. Hofmann, A.; Renee, K.; Christian, M. Handbook of Organic Materials for Electronic and Photonic Devices. In *Handbook of Organic Materials for Electronic and Photonic Devices*; Oksana, O., Ed.; Elsevier: Amsterdam, The Netherlands, 2019; pp. 429–449. ISBN 978-0-08-102284-9.
47. Gorbachev, R.V.; Riaz, I.; Nair, R.R.; Jalil, R.; Britnell, L.; Belle, B.D.; Hill, E.W.; Novoselov, K.S.; Watanabe, K.; Taniguchi, T.; et al. Hunting for Monolayer Boron Nitride: Optical and Raman Signatures. *Small* **2011**, *7*, 465–468. [CrossRef]
48. Schmitsdorf, R.F. Explanation of the Linear Correlation between Barrier Heights and Ideality Factors of Real Metal-Semiconductor Contacts by Laterally Nonuniform Schottky Barriers. *J. Vac. Sci. Technol. B Microelectron. Nanom. Struct.* **1997**, *15*, 1221. [CrossRef]
49. Ahmad, F.; Mansoori, A.; Bansal, S.; Dhahi, T.S.; Ahmad, S. Device Applications of Metal-2D-Materials Interfaces A Short Review. *Eur. J. Eng. Res. Sci.* **2018**, *3*, 1. [CrossRef]
50. Ahmad, S. *Microwave and Millimetre Wave Semiconductor Materials Technology*; Tata Mcgraw-hill Publishing Company Limited: New Delhi, India, 1998.
51. Wang, S.; Yu, Z.; Wang, X. Electrical Contacts to Two-Dimensional Transition-Metal Dichalcogenides. *J. Semicond.* **2018**, *39*, 1–8. [CrossRef]
52. Byun, K.E.; Chung, H.J.; Lee, J.; Yang, H.; Song, H.J.; Heo, J.; Seo, D.H.; Park, S.; Hwang, S.W.; Yoo, I.; et al. Graphene for True Ohmic Contact at Metal-Semiconductor Junctions. *Nano Lett.* **2013**, *13*, 4001–4005. [CrossRef]
53. Qiu, D.; Kim, E.K. Electrically Tunable and Negative Schottky Barriers in Multi-Layered Graphene/MoS 2 Heterostructured Transistors. *Sci. Rep.* **2015**, *5*, 13743. [CrossRef]
54. Liu, Y.; Wu, H.; Cheng, H.C.; Yang, S.; Zhu, E.; He, Q.; Ding, M.; Li, D.; Guo, J.; Weiss, N.O.; et al. Toward Barrier Free Contact to Molybdenum Disulfide Using Graphene Electrodes. *Nano Lett.* **2015**, *15*, 3030–3034. [CrossRef] [PubMed]
55. Yang, H.; Heo, J.; Park, S.; Song, H.J.; Seo, D.H.; Byun, K.E.; Kim, P.; Yoo, I.K.; Chung, H.J.; Kim, K. Graphene Barristor, a Triode Device with a Gate-Controlled Schottky Barrier. *Science* **2012**, *336*, 1140–1143. [CrossRef]
56. Choi, B.K.; Ulstrup, S.; Gunasekera, S.M.; Kim, J.; Lim, S.Y.; Moreschini, L.; Oh, J.S.; Chun, S.H.; Jozwiak, C.; Bostwick, A.; et al. Visualizing Orbital Content of Electronic Bands in Anisotropic 2D Semiconducting ReSe2. *ACS Nano* **2020**, *14*, 7880–7891. [CrossRef]
57. Leicht, G.; Berger, H.; Levy, F. The Growth of N- and p-Type ReS2 and ReSe2 Single Crystals and Their Electrical Properties. *Solid State Commun.* **1987**, *61*, 531–534. [CrossRef]
58. Zhao, Q.; Jie, W.; Wang, T.; Castellanos-Gomez, A.; Frisenda, R. InSe Schottky Diodes Based on Van Der Waals Contacts. *Adv. Funct. Mater.* **2020**, *30*, 2001307. [CrossRef]
59. Rose, A. *Concepts in Photoconductivity and Allied Problems*, 2nd ed.; Robert E. Krieger Publishing Co.: Huntington, New York, NY, USA, 1978.
60. Han, X.; Xing, J.; Xu, H.; Huang, Y.; Li, D.; Lu, J.; Li, P.; Wu, Y. Remarkable Improved Photoelectric Performance of SnS2 Field-Effect Transistor with Au Plasmonic Nanostructures. *Nanotechnology* **2020**, *31*, 215201. [CrossRef] [PubMed]
61. Claro, M.S.; Grzonka, J.; Nicoara, N.; Ferreira, P.J.; Sadewasser, S. Wafer-Scale Fabrication of 2D β-In2Se3 Photodetectors. *Adv. Opt. Mater.* **2021**, *9*, 2001034. [CrossRef]
62. Kim, J.; Heo, K.; Kang, D.H.; Shin, C.; Lee, S.; Yu, H.Y.; Park, J.H. Rhenium Diselenide (ReSe2) Near-Infrared Photodetector: Performance Enhancement by Selective p-Doping Technique. *Adv. Sci.* **2019**, *6*, 1901255. [CrossRef] [PubMed]
63. Buscema, M.; Island, J.O.; Groenendijk, D.J.; Blanter, S.I.; Steele, G.A.; Van Der Zant, H.S.J.; Castellanos-Gomez, A. Photocurrent Generation with Two-Dimensional van Der Waals Semiconductors. *Chem. Soc. Rev.* **2015**, *44*, 3691–3718. [CrossRef]
64. Thomas, P. *Pearsall Photonic Essentials*, 1st ed.; Tata Mcgraw-Hill Publishing Company Limited: New Delhi, India, 2003.
65. Cui, F.; Li, X.; Feng, Q.; Yin, J.; Zhou, L.; Liu, D.; Liu, K.; He, X.; Liang, X.; Liu, S.; et al. Epitaxial Growth of Large-Area and Highly Crystalline Anisotropic ReSe2 Atomic Layer. *Nano Res.* **2017**, *10*, 2732–2742. [CrossRef]
66. Wang, X.; Huang, L.; Peng, Y.; Huo, N.; Wu, K.; Xia, C.; Wei, Z.; Tongay, S.; Li, J. Enhanced Rectification, Transport Property and Photocurrent Generation of Multilayer ReSe2/MoS2 p–n Heterojunctions. *Nano Res.* **2016**, *9*, 507–516. [CrossRef]
67. Elahi, E.; Khan, M.F.; Rehman, S.; Khalil, H.M.W.; Rehman, M.A.; Kim, D.K.; Kim, H.; Khan, K.; Shahzad, M.; Iqbal, M.W.; et al. Enhanced Electrical and Broad Spectral (UV-Vis-NIR) Photodetection in a Gr/ReSe2/Gr Heterojunction. *Dalt. Trans.* **2020**, *49*, 10017–10027. [CrossRef]

68. Ali, M.H.; Kang, D.-H.; Park, J.-H. Rhenium Diselenide (ReSe2) Infrared Photodetector Enhanced by (3-Aminopropyl)Trimethoxysilane (APTMS) Treatment. *Org. Electron.* **2018**, *53*, 14–19. [CrossRef]
69. Yang, S.; Tongay, S.; Yue, Q.; Li, Y.; Li, B.; Lu, F. High-Performance Few-Layer Mo-Doped ReSe2 Nanosheet Photodetectors. *Sci. Rep.* **2014**, *4*, 1–6. [CrossRef]
70. Liu, F.; Zheng, S.; Chaturvedi, A.; Zólyomi, V.; Zhou, J.; Fu, Q.; Zhu, C.; Yu, P.; Zeng, Q.; Drummond, N.D.; et al. Optoelectronic Properties of Atomically Thin ReSSe with Weak Interlayer Coupling. *Nanoscale* **2016**, *8*, 5826–5834. [CrossRef]
71. Ishigami, M.; Chen, J.H.; Cullen, W.G.; Fuhrer, M.S.; Williams, E.D. Atomic Structure of Graphene on SiO 2. *Nano Lett.* **2007**, *7*, 1643–1648. [CrossRef]
72. Ando, T. Screening Effect and Impurity Scattering in Monolayer Graphene. *J. Phys. Soc. Japan* **2006**, *75*, 074716. [CrossRef]
73. Fratini, S.; Guinea, F. Substrate-Limited Electron Dynamics in Graphene. *Phys. Rev. B Condens. Matter Mater. Phys.* **2008**, *77*, 195415. [CrossRef]
74. Chen, J.H.; Jang, C.; Xiao, S.; Ishigami, M.; Fuhrer, M.S. Intrinsic and Extrinsic Performance Limits of Graphene Devices on SiO_2. *Nat. Nanotechnol.* **2008**, *3*, 206–209. [CrossRef]
75. Castro Neto, A.H.; Guinea, F.; Peres, N.M.R.; Novoselov, K.S.; Geim, A.K. The Electronic Properties of Graphene. *Rev. Mod. Phys.* **2009**, *81*, 109–162. [CrossRef]
76. Xue, J.; Sanchez-Yamagishi, J.; Bulmash, D.; Jacquod, P.; Deshpande, A.; Watanabe, K.; Taniguchi, T.; Jarillo-Herrero, P.; Leroy, B.J. Scanning Tunnelling Microscopy and Spectroscopy of Ultra-Flat Graphene on Hexagonal Boron Nitride. *Nat. Mater.* **2011**, *10*, 282–285. [CrossRef]
77. Meric, I.; Han, M.Y.; Young, A.F.; Ozyilmaz, B.; Kim, P.; Shepard, K.L. Current Saturation in Zero-Bandgap, Top-Gated Graphene Field-Effect Transistors. *Nat. Nanotechnol.* **2008**, *3*, 654–659. [CrossRef]
78. Duan, J.; Wang, X.; Lai, X.; Li, G.; Watanabe, K.; Taniguchi, T.; Zebarjadi, M.; Andrei, E.Y. High Thermoelectricpower Factor in Graphene/HBN Devices. *Proc. Natl. Acad. Sci. USA* **2016**, *113*, 14272–14276. [CrossRef]